Siddique et al. *NPG Asia Materials* (2023)15:36
https://doi.org/10.1038/s41427-023-00483-y

NPG Asia Materials

ARTICLE Open Access

Diamond-structured nanonetwork gold as mechanical metamaterials from bottom-up approach

Suhail K. Siddique[1], Hassan Sadek[1], Chi-Wei Wang[2], Chang-Chun Lee[2], Cheng-Yuan Tsai[3], Shou-Yi Chang[3], Chia-Lin Li[4], Chun-Hway Hsueh[4] and Rong-Ming Ho[1]

Abstract

Herein, this work aims to develop a facile method for the fabrication of metallic mechanical metamaterial with a well-ordered diamond structure from a bottom-up approach using a self-assembled block copolymer for templated electrochemical deposition. By controlling the effective volume fraction of PDMS in PS-*b*-PDMS *via* solvent annealing followed by HF etching of PDMS, it is feasible to obtain nanoporous PS with diamond-structured nanochannels and used it as a template for templated electrochemical deposition. Subsequently, well-ordered nanonetwork gold (Au) can be fabricated. As evidenced by nanoindentation and micro-compression tests, the mechanical properties of the diamond-structured Au after removal of PS give the combination of lightweight and mechanically robust characteristics with an exceptionally high reduced elastic modulus of 11.9 ± 0.6 GPa and yield strength of 193 ± 11 MPa above the Hashin-Shtrikman upper bound of 72 MPa with a bending-dominated structure at equivalent density. The corresponding deformation mechanism can be elucidated by morphological observations experimentally and finite element analysis (FEA) numerically. This work demonstrates the bottom-up approach to fabricating metallic monolith with diamond structure in the nanoscale, giving a superior performance as mechanical metamaterials.

Introduction

Historically, the creation of lightweight cellular materials with mechanically robust characteristics has been the most sought-after engineering pursuit. The idea to explore mechanical properties with characteristic cellular architectures emerged from various lightweight biological systems such as bone[1], sea urchins[2], knobby starfish[3], and nacre[4]. Inspired by these natural cellular materials, a new paradigm in material science has emerged for fabricating artificial cellular materials possessing various topologies for a wide range of applications[5]. According to the complexity and structural features, cellular materials are categorized into strut-based open-cellular networks or bending-dominated structures with strength factor $\rho^{3/2}$ and surface-based closed-cellular networks or stretching-dominated structures with strength factor ρ[6].

Recent progress in material science for the fabrication of architectural materials can explore and extend the structure-property relationship. Despite their geometrical complexity, it is possible to fabricate well-ordered cellular architectures with a variety of structures using a top-down method like additive manufacturing (3D printing and interference lithography). By taking advantage of the deliberate structuring effect it is possible to create a superior mechanical performance with lower density by fabricating hierarchical network structures[7,8]. On the definition of metamaterials by Pendry et al.[9,10], the materials whose effective properties are not from the bulk behavior of the materials that are composed it but mainly from their deliberate structuring. Those artificially engineered structures with the character of

Correspondence: Rong-Ming Ho (rmho@mx.nthu.edu.tw)
[1]Department of Chemical Engineering, National Tsing Hua University, Hsinchu 30013, Taiwan
[2]Department of Power Mechanical Engineering, National Tsing Hua University, Hsinchu 30013, Taiwan
Full list of author information is available at the end of the article

metamaterials offer unique emergent properties like high stiffness, negative Poisson's ratio, and specific energy absorption[7,11,12]. However, the stochasticity and structural inhomogeneity in such structural features can predominantly reduce mechanical properties due to the reduction of density. Moreover, the manipulation of architectural features in the nanoscale for the fabrication of mechanical metamaterials remains challenging. Note that recent advances in the top-down methods are reaching 400–500 nm[13]. For octa-truss structured carbon fabricated by the top-down method, the theoretical strength of glassy carbon can be achieved by reducing the size of the ligament as studied by Bauer et al.[14]. It is reasonable to expect that further reduction of ligament size to tens of nanometer scale can be able to exhibit superior properties due to the nanosized effect. In fact, the fabrication of cellular structures with nanoscale ligaments has been reported to exhibit high mechanical properties due to the nanosized effect, where nanosized ligaments in network structures play a vital role in enhanced mechanical properties[15,16]. As demonstrated by the dealloying approach, it is possible to reach the theoretical strength of nano ligament Au[17]. Yet, the fabrication of well-ordered hierarchical structures by the top-down approach is still limited due to their constraint to go beyond the submicron length scale; also, the top-down approach might not be cost-effective for material fabrication.

In the past decade, mechanical metamaterials using metallic materials have gained immense attention due to the novel design principles, which combine with the material size effect at the micro/nanoscale and topology effect of well-ordered texture, giving the combined effect of nanosize and architecture on mechanical properties. Depending on their material characteristics and nanostructures, the nanonetwork metals with hollow struts can show exceptional properties such as low relative density, high mechanical properties, and enhanced plasmonic behavior[18–21]. However, the hollow metallic micro/nanolattice exhibits low strength due to the significant reduction in their density[22,23], leading to poor energy absorption capability. Note that recent advances in the 'bottom-up approach' can generate deliberately structured materials, which help to improve the fabrication of nanonetwork structures. More precisely, the evolution of metamaterials made from a bottom-up approach or self-assembly seek to develop entirely new or significantly enhanced properties by rational design[24]. Recently, block copolymers (BCPs) have been extensively investigated due to their ability to self-assemble into a variety of periodic nanostructures depending on their molecular weights and constituent compositions[25,26]. Among them, diamond structure finds a prominent position due to their unique nanonetwork structure with tetrapod texture for high mechanical properties[27–29]. Indeed, the mechanical enhancement from the deliberate structuring of nanonetwork textures will be strongly dependent upon the number of struts and nanosized ligaments in an isotropic periodic structure. As demonstrated in our previous work, the diamond structure with four struts is better than the gyroid structure with three struts due to the higher capability to distribute the loading stress[28]. Recently, the fabrication of nanonetwork materials using bottom-up approaches has been developed using a polymer template by atomic layer deposition, electroless plating, sol-gel reaction, and electro-deposition[30–34].

Herein, this work aims to demonstrate the mechanical characteristics of a well-ordered nanonetwork gold (Au) with tens of nanometer scale struts (25 nm) (the smallest strut size for mechanical metamaterials so far) from a cost-effective method fabricated by a bottom-up approach using self-assembled polystyrene-*b*-polydimethylsiloxane (PS-*b*-PDMS) with diamond structure as a template for templated electrochemical deposition. As illustrated in Fig. 1, the network phase with a diamond structure in the nanoscale can be acquired through the self-assembly of PS-*b*-PDMS. The PDMS block can be selectively etched using hydrofluoric acid (HF), and a diamond-structured PS template can be fabricated. Subsequently, the fabricated well-ordered nano-channeled PS can be used as a template for templated electrochemical deposition using a cyanide-based electrolyte. Accordingly, after the removal of the PS template, nanonetwork metallics with free-standing characteristics can be fabricated, particularly in

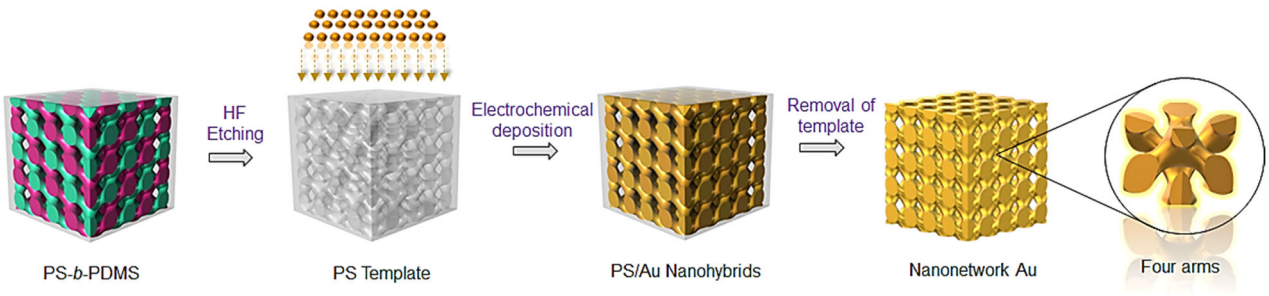

Fig. 1 Design and fabrication process. Schematic illustration for fabrication of well-ordered nanonetwork Au from a bottom-up approach.

the thin-film state. By taking advantage of this bottom-up approach, it is feasible to fill the material property chart by Gibson and Ashby with enhanced performance. A systematic representation of "diamond structure" in mechanical properties using a bottom-up approach has not been reported before. Moreover, the top-down approach for the fabrication of a well-ordered micro-truss or octa-truss cannot reach the nanosized effect to show the "smaller the stronger" behavior for a bending-dominated structure but it can be achieved by the demonstrated approach in this study. This bottom-up approach for the fabrication of well-ordered nanonetwork metallic (Au) nanonetwork should provide complementary knowledge for fabricating low-density materials with superior mechanical performances resulting from the deliberate structuring with nanosized texture and a high degree of order.

Methods and materials

Materials

The PS-*b*-PDMS block-copolymer was synthesized by anionic polymerization, which was described in our previous publications. The PS-*b*-PDMS used in this study has a total molecular weight of 86,000 g/mol ($\bar{M}_n^{PS}$: 51,000 g/mol; $\bar{M}_n^{PDMS}$: 35,000 g/mol). The diamond-structured PS template nanochannels were fabricated by solvent annealing followed by Hydrofluoric acid (Sigma Aldrich) etching. The electrochemical deposition was performed using a cyanide-based aqueous electrolyte from Potassium dicyanoaurate (I) (Sigma Aldrich).

PS-*b*-PDMS self-assembled monolith fabrication

The BCP thin film (monolith) can be fabricated by dip coating using 10 wt % of PS-*b*-PDMS solution in chloroform. The controlled retraction of the silicon wafer through the precursor solution can result in a thin film of PS-*b*-PDMS in the silicon wafer. Moreover, the thickness of the film can be controlled using the concertation of the solution and the withdrawing rate of the silicon wafer. The fabricated film was dried at 50°C for 1 h. By taking advantage of the solvent annealing apparatus, it is possible to acquire desired morphology using PS selective solvent (Chloroform). By using the solvent annealing apparatus, it is possible to control the solvent flow rate and the nitrogen purge flow. With the use of selective solvent, the swelling behavior of the PS block can be varied, and eventually, the effective volume fraction of PDMS (f_{PDMS}^{eff}) can be reduced to 0.35. After solvent annealing with chloroform at the flow rate of 20 ml/min for 30 h a well-ordered diamond structure PS-*b*-PDMS can be formed. Selective etching of PDMS using hydrofluoric (HF) acid from PS-*b*-PDMS to fabricate nanoporous diamond-structured PS as templates and collected to an Indium Tin Oxide (ITO) substrate for templated electrochemical deposition of Au.

Templated electrochemical deposition of Au

The precursor solution for electrochemical deposition was prepared using 1 g of Potassium dicyanoaurate (I) (Sigma Aldrich) dissolved in 50 ml of methanol. The electrochemical deposition of Au can occur by a simple faradaic reaction with direct reduction of metal ions. An electrochemical cell consisting of Ag/AgCl as a reference electrode and a platinum mesh as a counter electrode was used for the reaction. A small molecular-weight solvent like methanol was used as a surfactant for the infiltration of aqueous electrolytes. The electro-deposition was performed with cyclic voltammetry from −1.8 V to −0.5 V versus Ag/AgCl as a reference electrode. Gold metal was deposited at room temperature at a potential of −1.4 V. After the deposition, the samples are rinsed with methanol and water and then dried at 50 °C for 12 h. The PS template can be simply dissolved by an organic solvent. In this study, styrene (monomer of PS) was applied as a solvent to remove the PS template. After treatment with styrene for 12 h, the PS template can be slowly dissolved. Subsequently, the nanoporous Au was vacuum-dried overnight to remove the residual styrene.

Nanoindentation measurements

For the mechanical characterization, a nanoindentation (Hysitron Ti950 triboindenter) measurement with calibrated Berkovich and spherical indenter with a diameter of 2 μm was used. The load-displacement (P-h) curve for mechanical measurements was conducted using both the intenders on a metallic monolith sample with a thickness of 3.2 μm at room temperature. For consistency of results, the indentation data were obtained after applying different loads with a maximum load of 400 μN, 600 μN, 800 μN, 1000 μN, and 1200 μN at the same loading and unloading rate (60 μN/s). The stiffness of the indented samples was calculated using the initial slope of the unloading curve $S = dP/dh$. The reduced elastic modulus of the samples was calculated using the Oliver-Pharr model.

$$Er = \frac{\sqrt{\pi}}{2}\frac{S}{\sqrt{A_t}}$$

Here E_r is reduced elastic modulus (indentation modulus) which represents the elastic deformation that occurs in both the sample and indenter tip. S is stiffness. A_t represents the projected contact area.

Uniaxial micro-compression

The fabrication of the pillar for micro-compression was performed using a dual beam FIB milling machine (Helios NanoLab 600, FEI) with FESEM analysis attached to it. The FIB was conducted in two steps: the surrounding area of the micropillars was fabricated by fast milling (30 kV, 0.44 nA) followed by slow milling (30 kV, 9.7pA) for final

cutting to reduce the beam damage, eventually giving a well-defined pillar with a diameter of 2.4 μm and 3.2 μm height. SEM imaging was taken at 52° tilt at 5 kV in the immersion mode. By taking advantage of careful milling of Au nanonetwork at a lower current, it is possible to minimize the defects as further confirmed by the FESEM image. By using a 10 μm diameter flat indenter was used to apply compressive stress to the fabricated pillar until the strain hardening. The engineering stress can be calculated from the load at a specific area, whereas the engineering strain can be calculated using displacement with respect to the height of the pillar. The yield strength (σ_Y) can be considered as the transition between elastic and plastic deformation points.

Results and discussion

Diamond-structured nanonetwork gold (Au) *via* templated electrochemical deposition

By taking advantage of large interaction parameter, PS-*b*-PDMS block copolymer can be self-assembled into a geometrically complex diamond phase by using solvent annealing apparatus with controlled solvent annealing using PS selective solvent (Chloroform) for stable lamellae forming PS-*b*-PDMS[35]. Table S1 shows the sample information (PS-*b*-PDMS) used in this study[36]. As shown in Fig. S1, the characteristic development of diamond structure from as-cast PS-*b*-PDMS was studied by FESEM analysis. Primarily, the as-cast PS-*b*-PDMS shows network structure without any particular order as shown in Fig. S1a; eventually, after solvent annealing using chloroform for 15 h at the flow rate of 20 ml/min, a partially ordered diamond-structured PS-*b*-PDMS can be obtained (Fig. S1b). Consequently, after annealing at the flow rate of 20 ml/min for 30 h a well-ordered diamond-structured PS-*b*-PDMS can be acquired as shown in Fig. S1c. Furthermore, the morphological evolution of PS-*b*-PDMS can be reaffirmed by the 1D SAXS profile (Fig. S1d). A primary peak can be obtained from the SAXS pattern for the short range ordered texture as shown in Fig. S1d(i). As exemplified in Fig. S1d(ii), the characteristic primary peak shifted towards the low-q region after solvent annealing with chloroform at the flow rate of 20 ml/min for 15 h. Furthermore, gradual increase in the annealing time for solvent annealing with a flow rate of 20 ml/min for 30 h, clear scattering peaks with the relative q values at $\sqrt{2}$:$\sqrt{3}$:$\sqrt{4}$: $\sqrt{6}$: $\sqrt{8}$: $\sqrt{14}$: $\sqrt{18}$: $\sqrt{22}$ were obtained as shown in Fig. S1d(iii), which reaffirms the FESEM analysis of the double diamond phase. Note that the primary peak of the disordered state should be different from the one with the developed texture of the ordered phase so that it might not be appreciated to compare the results between disordered and ordered ones. As a result, with the use of a PS selective solvent (chloroform) for solvent annealing, it is possible to acquire the DD-structured monolith as shown in Fig. S1c, with the least structural defects but reasonable long-range ordering. By taking advantage of hydrofluoric acid etching, diamond-structured nanochannels can be acquired as a template for templated electrochemical deposition of gold.

In general, the electrochemical deposition of metals through the nanochannels of template might encounter a variety of difficulties for pore-filling. For a better electrochemical deposition of gold, an inert platinum (Pt) electrode was used as a counter electrode and Ag/AgCl as a reference electrode. With the use of cyanide-based electrolytes, pore filling of the aqueous solution of Au ion into the nanochannels of the PS template can be ensured. The electrochemical deposition of Au characteristically involves a faradaic reaction with a direct reduction of metal cations in the cathode to yield the preferred deposition of Au into the nanochannels. Moreover, considering the slow reduction rate, multiple cyclic voltammetry was used to ensure the complete pore filling of nanochannels (Fig. 2a). In contrast to the electrodeposition of metal oxides and hydroxides, metal electrochemical deposition involves the reduction of metal without any intermediate reactions. For better disposition characteristics, as shown in Fig. 2b, multiple cyclic voltammetry for electrochemical deposition was conducted from −1.8 V to −0.5 V versus Ag/AgCl as a reference electrode. Considering the successive cyclic voltammetry, the reduction of Au metal ions will occur at −1.4 V (Fig. 2b). Subsequently, successive reduction proceeds without any intermediate reactions involved, which favors a compact deposition; note that for a successful pore-filling process, a suitable solvent like ethanol should be used to enhance the accessibility of electrolytes toward PS template nanochannels. The initial deposition starts with a nonuniform metal layer after five cycles of CV as shown in Fig. 2c. However, with the gradual increase in the number of cycles (20 cycles) for electrochemical deposition, a uniform layer of reduced Au can be deposited on the ITO substrate as shown in Fig. 2d. Moreover, after fifty cycles of CV, well-developed Au nanonetworks in the PS template can be obtained by controlling the accumulation rate. The electrochemical reaction would be stopped before the overgrowth. By controlling the Au accumulation rate, a uniform diamond-structured Au in the PS matrix as a monolith can be successfully fabricated. The fabricated samples were rinsed with methanol and washed using deionized water, then dried at 50 °C for 12 h. Furthermore, the fabricated samples were electively freed from the PS template by the dissolution of the PS phase using styrene monomer. As shown in Fig. 2f, the diamond-structured Au can be fabricated with two interpenetrated single diamond nanonetworks; note that the least shifting of nanonetworks can be observed after the removal of the template (see inset of Fig. 2e).

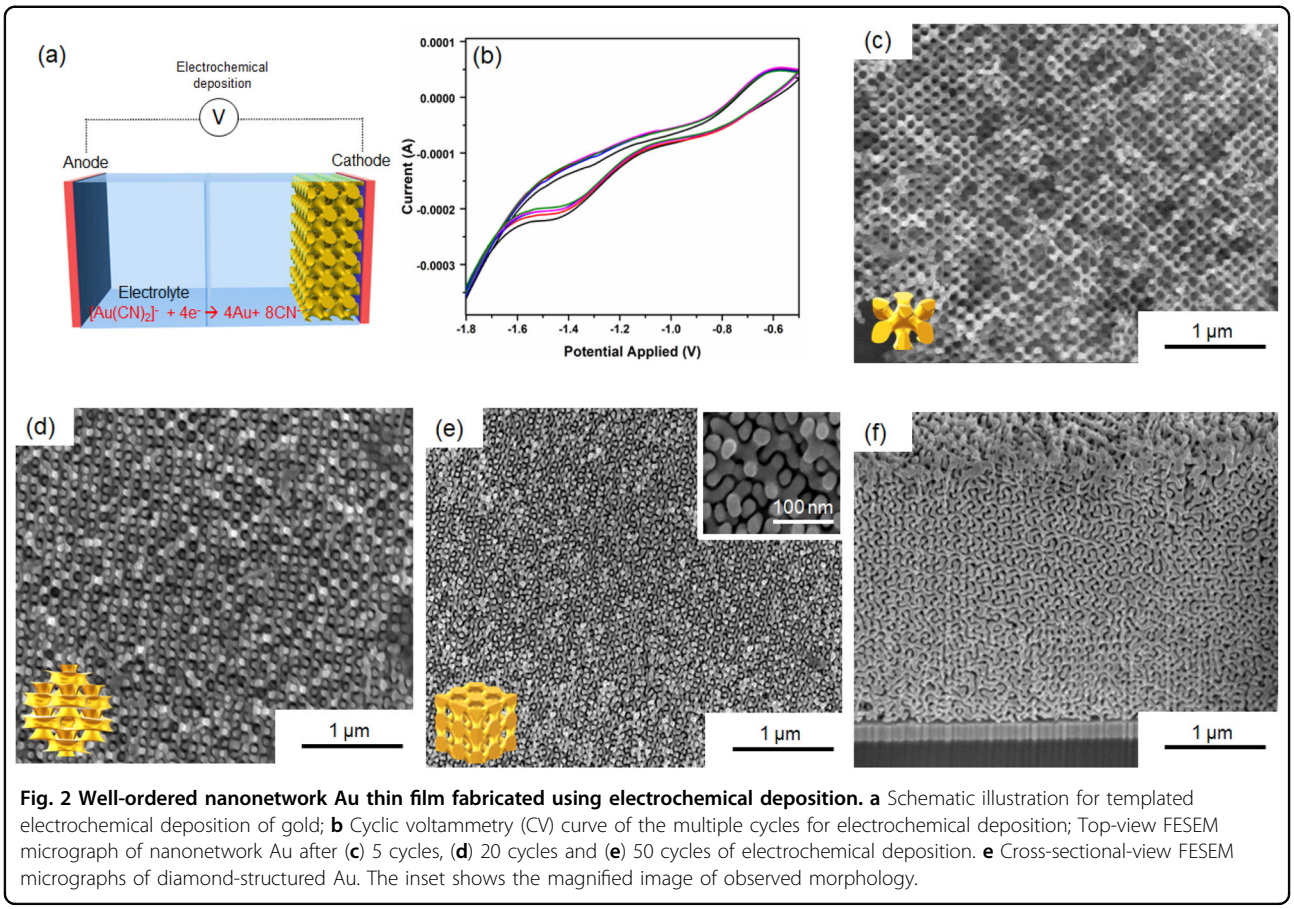

Fig. 2 Well-ordered nanonetwork Au thin film fabricated using electrochemical deposition. a Schematic illustration for templated electrochemical deposition of gold; **b** Cyclic voltammetry (CV) curve of the multiple cycles for electrochemical deposition; Top-view FESEM micrograph of nanonetwork Au after (**c**) 5 cycles, (**d**) 20 cycles and (**e**) 50 cycles of electrochemical deposition. **e** Cross-sectional-view FESEM micrographs of diamond-structured Au. The inset shows the magnified image of observed morphology.

Moreover, the fabricated Au nanonetwork with a thickness of ~3.2 μm, as evidenced by the cross-sectional-view FESEM imaging (Fig. 2f), can be used for a comprehensive study of mechanical properties. Accordingly, the multiple cycles of cyclic voltammetry can gradually deposit the reduced gold into the template. However, for the mechanical characterization, it is necessary to avoid overgrowth deposition over the template to preserve the diamond structure for the nanoindentation test. By taking advantage of cyclic voltammetry, it is possible to control the deposition rate in an electrochemical deposition. As a result, a well-controlled thickness of diamond-structured Au can be possible for the mechanical test.

The fabricated diamond-structured nanonetwork Au can be confirmed by the FESEM micrograph as demonstrated above. To reaffirm the nanostructured Au, one-dimensional small-angle X-ray scattering (1D SAXS) was acquired to further examine the observed morphology. As shown in Fig. S3a, the characteristic reflections at relative q values of $\sqrt{2}$:$\sqrt{3}$:$\sqrt{4}$:$\sqrt{6}$ can be identified (red line) for double diamond-structured Au. An appearance of an additional peak (blue line) is attributed to the shifting of double-diamond network geometry after removal of the template, which shows $\sqrt{3}$ peak of a single diamond-like structure. Moreover, a wide-angle X-ray diffraction pattern was used to examine the crystalline Au with a diamond-structured texture. As shown in Fig. S3b, the diffraction peaks of 2θ at 38.31° (111), 44.46° (200), 64.67° (220), 77.45° (311), and 83.3° (222) suggest that the diamond-structured gold is identified as a crystalline phase with face-centered cubic (FCC) lattice. Note that those additional diffraction peaks of 2θ at 30.85°, 51.02° and 60.66° (Fig. S3b) are the results from the indium tin oxide (ITO) with crystalline planes of (400), (440), and (622), respectively. As a result, the templated electrochemical deposition of cyanide-based electrolytes gives the formation of highly crystalline gold. The diamond-structured Au was further characterized by using FESEM-EDS with corresponding elemental mapping as exemplified in Fig. S4. Moreover, Fig. S4b and S4c show the elemental mapping and corresponding EDS-spectra, respectively, which shows the pure Au after reduction without any further reactions. Indeed, the results are in line with the suggested crystalline Au with a diamond-structured texture. The fabricated nanonetwork Au is in the highly crystalline FCC form with diamond nanonetworks. Accordingly, the superior mechanical properties of the diamond-structured Au including elastic modulus and

yield strength are from the highly crystalline state with strong metallic bonding instead of an amorphous one.

Mechanical characterization of diamond-structured Au

The mechanical properties of the well-ordered nanonetwork Au were investigated using a nanoindentation test fitted with a calibrated Berkovich indenter in Hysitron Ti950 triboindenter (Hysitron Inc. Minneapolis, MN, USA.). Note that the Berkovich intender has included angle of 142.3° and a half angle of 65.27°. Primarily, the indentation measurements with a maximum load of 400 μN were used to determine the mechanical properties of intrinsic (bulk) Au. As shown in Fig. S5, a typical load-displacement curve for intrinsic Au by nanoindentation can be acquired. Based on the unloading curve, a reduced elastic modulus (E_r) of intrinsic Au was determined as 76.6 GPa from the initial slop ($S = \mathrm{dp/dh}$), which is considered as stiffness from the unloading curve. For a comprehensive study on mechanical properties of the nanonetwork Au, the nanoindentation experiments were conducted with a maximum load of 400 μN, 600 μN, 800 μN, 1000 μN, and 1200 μN by using Berkovich indenter at the same rate of loading and unloading (60 μN/s).

As a result, the reduced elastic modulus of diamond-structured nanonetwork Au using the Berkovich indenter can be determined as 11.9 ± 0.6 GPa (Fig. 3a). Note that the maximum indentation depth by the Berkovich indenter was ~320 nm; the low retracting while unloading indicates the occurrence of plastic deformation for the diamond-structured Au as compared to stiffer intrinsic Au as shown in Fig. S5. To acquire reliable results for reduced elastic modulus and corresponding deformation mechanism, further nanoindentation experiments were conducted using a spherical indenter with a diameter of 2 μm (Fig. 3b). The calculated reduced elastic modulus using the spherical indenter was ~12.3 ± 0.8 GPa, reaffirming the results obtained from the Berkovich indenter. Herein, the scaling law proposed by Gibson and Ashby for open-cell network materials (i.e., the open cellular bending-dominated structure) is typically used to semi-quantitatively describe the distinctive relationship between structure and property[37]. The effective Young's modulus of the strut-based structures can be expressed in terms of relative density, $E_r/E_s \approx \left(\rho/\rho_s\right)^2$ where E_r is the Young's modulus of metallic nanolattice, E_s is Young's modulus of intrinsic materials, and $\left(\rho/\rho_s\right)^2$ represents the relative density of cellular materials. Moreover, the relative density of diamond-structured Au was calculated as $\overline{\rho}^{DD} \sim 0.35$ with respect to the volume fraction of PDMS in the PS-*b*-PDMS ($f_{\mathrm{PDMS}}{}^{v}$) (i.e., the etching out constituent). Note that PS-selective solvent was used to fabricate the PS-*b*-PDMS self-assembled film with network phase from the intrinsic lamellar phase[35]. The effective volume fraction was thus calculated; note that the swelling mainly occurs in the PS domain as found. With the good preservation of the templated texture (PDMS nanonetwork), the volume fraction of the nanonetwork Au fabricated is expected to be approximately equal to the one from the PDMS (the pore volume after HF etching of PDMS in the PS-*b*-PDMS). Subsequently, the relative density was confirmed by the FESEM micrograph at which the diameter of the strut shows approximately equal size to the nanonetwork of the PDMS in the PS-*b*-PDMS (Fig. S6). By taking advantage of a strut-based, bending-dominated diamond structure, the expected modulus value for ideal cellular materials can be calculated as ~8.89 GPa for the nanonetwork Au with a relative density ($\overline{\rho}^{DD}$) around 0.35. Interestingly, the diamond-structured Au fabricated show significantly high reduced elastic modulus with a value of 11.9 ± 0.6 GPa, which implies the nanonetwork Au with lightweight characteristics can show outstanding stiffness with lower density (Fig. 3c).

Note that there are no bending-dominated lattice materials that can show high stiffness based on scaling law except octet truss lattice due to the higher number of ligaments[38]. This enhanced mechanical property could be attributed to the combined effect of deliberate structuring and the nanosized effect. The highest achievable elastic modulus of porous cellular materials is limited by the scaling law[14,22,37,39,40]. Note that the material strength can be manipulated by fabricating nanonetwork materials with the nanosized effect as reported before[41]. Such a "smaller stronger behavior" has also been reported in polymer systems by Mieszala et al.[42] and ceramic systems by Li et al. as well as metallic systems by Khaderi et al.[15,43–46]. Similarly, the diamond nanonetwork Au fabricated by templated electrochemical deposition can show significant enhancement on elastic modulus with respect to density as compared to predicted values from bending dominated structure. Furthermore, the applied stress while loading might lead to the deformation of one strut where the isotropic periodicity and interconnected nanonetwork will be able to guard against the complete failure of the struts, resulting in high stiffness characteristics. Consequently, there will be an obvious topological effect on the performance of mechanical properties even though the material shows a bending-dominated structure (see below for details from numerical simulation). Furthermore, the deformation mechanism of the nanonetwork Au fabricated after the nanoindentation tests were investigated using FESEM imaging at residual indented locations. As shown in Fig. 4a, the deformation is indeed confined in the specific contact area while using the Berkovich tip; note that the neighboring regions after indentation remain undeformed without any crack propagation or ligament slips. Moreover, the nanonetwork struts have a slight bulge while loading due to compressive shearing. By increasing the load, the deformation by

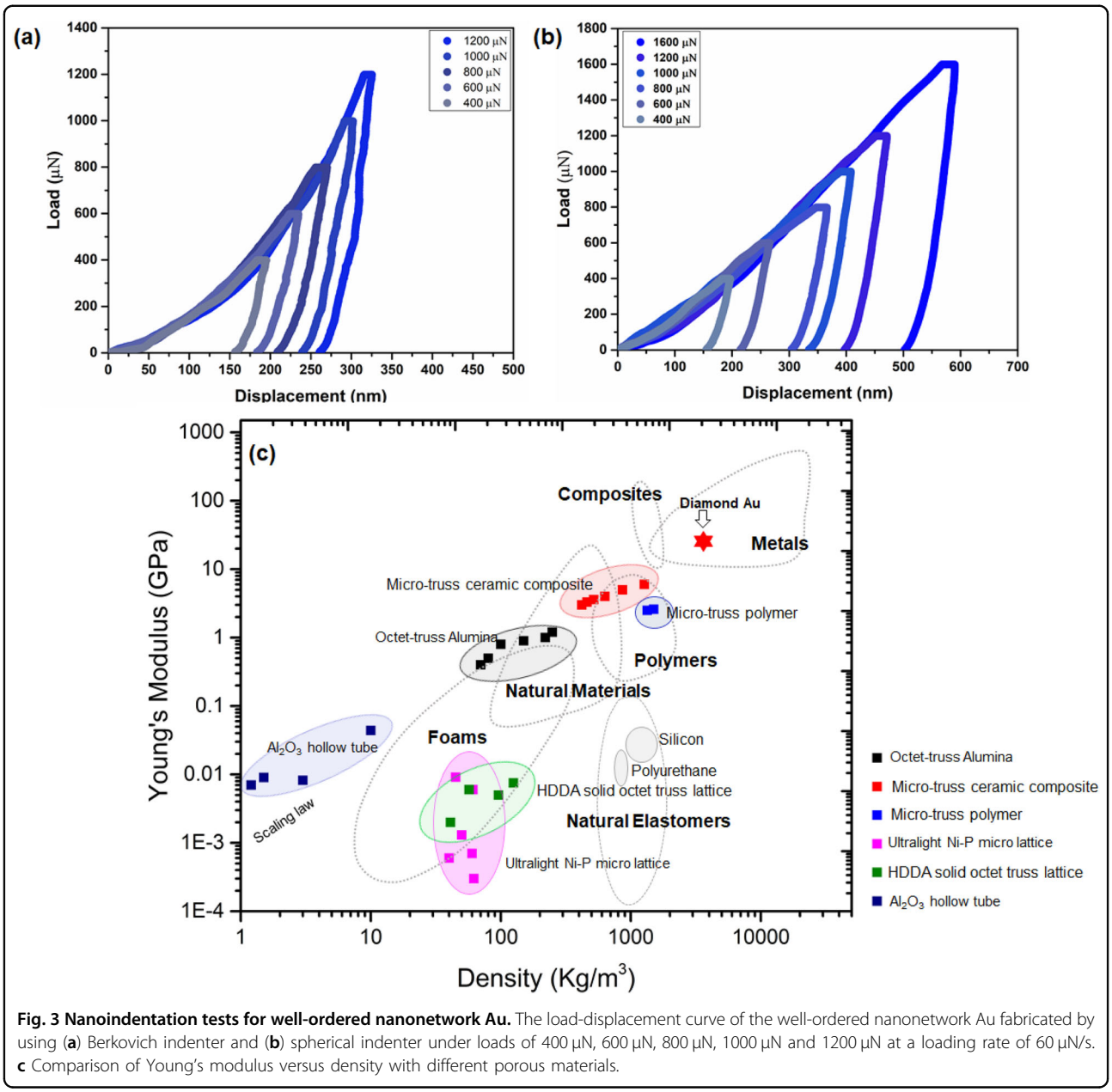

Fig. 3 Nanoindentation tests for well-ordered nanonetwork Au. The load-displacement curve of the well-ordered nanonetwork Au fabricated by using (**a**) Berkovich indenter and (**b**) spherical indenter under loads of 400 μN, 600 μN, 800 μN, 1000 μN and 1200 μN at a loading rate of 60 μN/s. **c** Comparison of Young's modulus versus density with different porous materials.

bulging can be prominent. As evidenced by the load-displacement curve (Fig. 3a, b), there is no specific retraction of the unloading curve to indicate the plastic mode of deformation, which is in line with deformation behavior at intended locations. Furthermore, the spherical indented location was also studied under FESEM micrograph; note that the further evaluation of post intended location of the spherical indenter also indicates local densification at the indented locations of diamond-structured Au without any ligament slips depicts a plastic mode of deformation as shown in Fig. S7.

To further examine the ligament deformation of nanonetwork struts under compression, cross-sectional-view FESEM with 52° tilt for imaging of milled samples by the focused ion beam (FIB) was studied. As shown in Fig. 4b, the initial deformation of the nanonetwork Au with the loading of 400μN suggests primary distortion by bending of the struts; note that the initial deformation of the struts will occur on a specific contact area under the tip without any substrate effect. Subsequently, after the initial bending, the plastic deformation can gradually lead to the buckling of the ligaments (Fig. 4c). Furthermore, the complete distortion of nanonetwork Au can occur after plastic bucking (Fig. 4d), which indicates that material failure can happen through the bending of the structs followed by buckling. To further examine the effect of deliberate

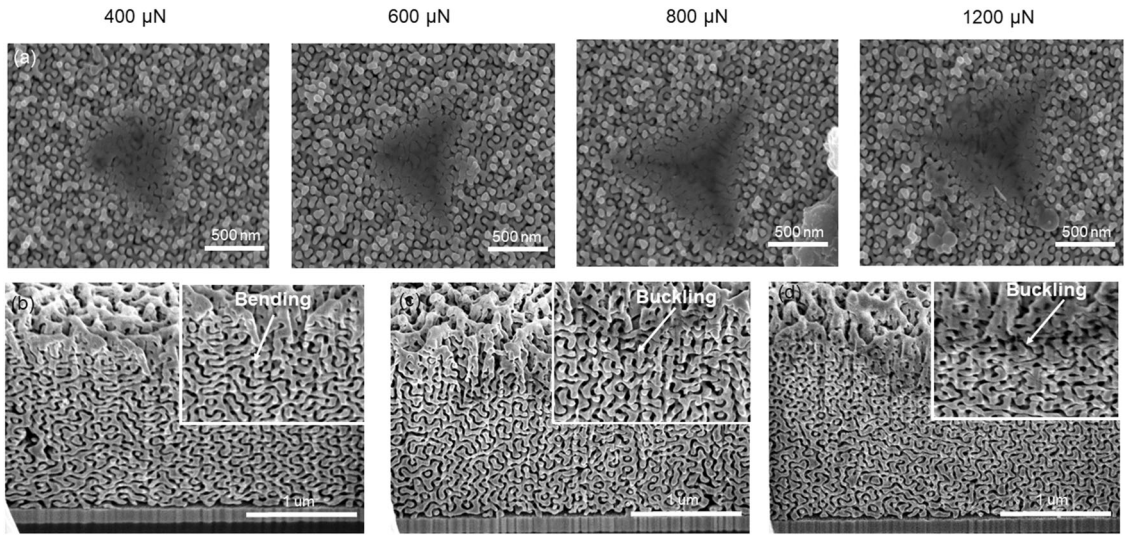

Fig. 4 Microscopic analysis of post-indentation locations. a FESEM micrographs of diamond-structured Au after nanoindentation using maximum loads of 400 μN, 600 μN, 800 μN, and 1200 μN with the use of Berkovich indenter. Cross-sectional-view SEM of diamond-structured Au after nanoindentation using spherical indenter with the maximum loads of (**b**) 400 μN (**c**) 800 μN and (**d**) 1600 μN.

structuring on the mechanical properties of the diamond-structured Au, a uniaxial micro-compression test was conducted on a micropillar with a well-defined compression volume. As shown in Fig. 5a for FESEM imaging with an angle of 52° tilt, a micropillar with a diameter of ~2.4 μm can be fabricated by FIB milling. By performing the micro-compression analysis using a flat indenter with a 10 μm diameter, it is feasible to provide comprehensive evidence of the stress-strain curve as shown in Fig. 5b; note that the load will be performed until strain hardening. For a systematic comparison, the micro-compression analysis was first performed for intrinsic non-structured Au. As shown in Fig. S8, the yield strength for intrinsic Au was calculated as 260 MPa; note that the yield strength for intrinsic gold according to the materials property chart was ~250–275 MPa.

Moreover, the intrinsic Au shows significant slips while loading as shown in Fig. S9a; where the failure of the material was predominantly by pillar slips. Interestingly, the failure of the nanonetwork Au occurs after a significant elastic limit with high yield strength at ~13% of strain; after that, complete plastic deformation can be evident. Interestingly, the plastic deformation of DD-structures Au starts from the shear bulging of the pillars without any pillar slips. As shown in Fig. S9b, the occurrence of shear bulging along the transverse direction of the load can be attributed to the bending of the struts followed by buckling after the elastic limit. Most interestingly, the yield strength (σ_Y) of the nanonetwork Au calculated from the stress-strain curve is ~193 ± 11 MPa.

The potential of nanonetwork materials to fill the vacant space in the Ashby plot was readily determined by employing "continuum" bounds on properties. By taking advantage of the density property chart of porous materials (Ashby plot) by Gibson and Ashby, the relationship between yield strength and relative density of cellular material can be given by $\sigma_{DD} = (\rho/\rho_s)^{3/2}\sigma_Y$ at relative density (ρ/ρ_s) where σ_Y and σ_{DD} indicate the yield strengths of intrinsic Au and the nanonetwork Au, respectively. The upper bound on the strength of an isotropic porous solid can be estimated using the non-linear Hashin–Shtrikman upper bound as shown in Eq. (1).

$$\frac{\sigma DD}{\sigma_Y} = \frac{2\overline{\rho}}{\sqrt{(1-\overline{\rho}) + 4[1 + 3/2(1-\overline{\rho})]}} \quad (1)$$

Note that there are few micro-structures of lattice materials that can be able to achieve the upper bound of the predicated results from the non-linear Hashin-Shtrikman model, yet the octet truss lattice is known to have theoretical properties that might be able to reach the upper limit. As shown in Fig. 5c, the yield strength (σ_Y) of the diamond-structured Au is ~268% larger than the expected value according to the Hashin-Shtrikman upper bound (72 MPa); note that the intrinsic Au shows a yield strength of ~260 MPa (Fig. S8).

Moreover, the yield strength of diamond-structured Au is two times higher than the previously reported nanoporous Au (90 MPa) by Biener et al. Furthermore, the diamond-structured nanonetwork Au shows significant enhancement in yield strength as compared to Ni-P hollow tube, Cu mesolattice, Al-Si10-Mg[47] and other nanoporous metals such as Cu and Au[17,22,38,40,43,48–53]. Accordingly, those results suggest the enhancement of the strength of the Au

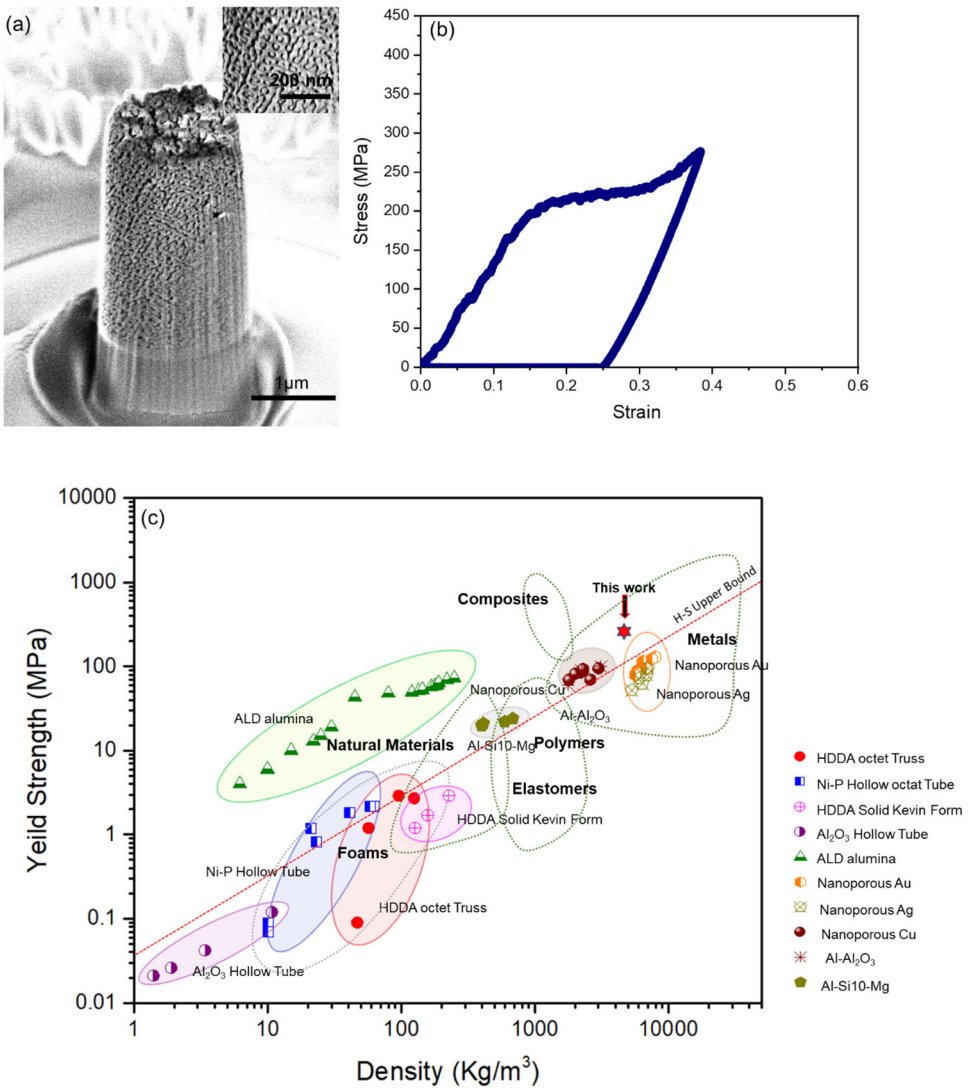

Fig. 5 Mechanical characterization of diamond-structured Au. a FESEM image of diamond-structured Au micropillar before uniaxial micro-compression. The inset shows the enlarged image of the sidewall of the micropillar. **b** Engineering stress-strain curves of diamond-structured Au. **c** Yield strength vs density material property chart comparing different porous metals with nanonetwork Au.

by the deliberate structuring even with lower density, in line with the concept of "smaller stronger behavior" reported by Biener et al.[43,52,54]. Moreover, the exceptional yield strength can be attributed to the combination of well- ordered diamond texture and well-interconnected nanosized struts, giving the synergistic effects from the topology of the well-ordered nanonetwork Au with the character of mechanical metamaterials. As shown in Fig. 5b, the deformation of the nanonetwork Au shows high yield strength at the beginning followed by plastic deformation.

Finite element analysis (FEA) of nanonetwork gold

To further explore the high mechanical properties and deformation mechanism of the well-ordered nanonetwork Au under equivalent stress, a numerical method for examining the strain distribution under the loading of diamond-structured Au models under nanoindentation was conducted by finite element analysis (FEA). The periodic boundary condition was applied for analysis using FEA. The mesh of the finite element model was provided as shown in Fig. 6a. The legends show von Mises stress/strain distribution of single unit cell for diamond structure. The unit for stress is Pa. As shown in Fig. 6b, the isometric view of von Mises stress shows that tends to maximize at the struts, reassuring the formation of deformation through the strut centers, which explains the microscopic failure confirmedly initiated from the struts rather than the nodes. Moreover, the stress distribution

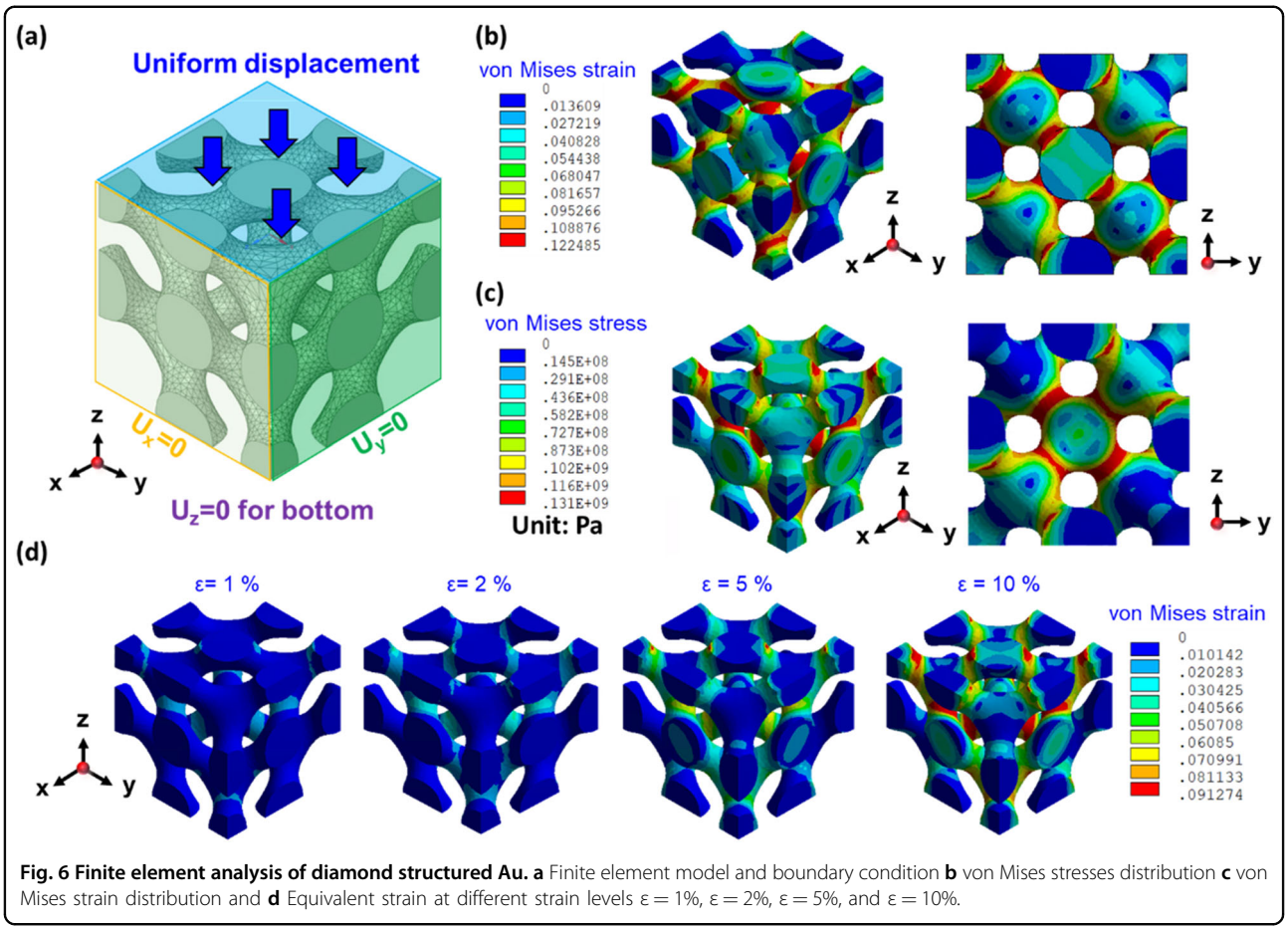

Fig. 6 Finite element analysis of diamond structured Au. a Finite element model and boundary condition **b** von Mises stresses distribution **c** von Mises strain distribution and **d** Equivalent strain at different strain levels ε = 1%, ε = 2%, ε = 5%, and ε = 10%.

happens at the whole strut reaching out to the center of the strut as shown in the 2D demonstration, giving the plastic deformation of the strut (Fig. 6c). Note that the applied loading could lead to the failure of one strut, giving neighboring struts start to involve guarding against complete failure of a collective network system, giving high elastic modulus and yield strength. As a result, the diamond-structured Au can be able to prevent effective failure that result from the slips as for the intrinsic Au; instead, plastic deformation can be dominated without slipping. Accordingly, the von Mises strain ($\varepsilon_{\text{von Mises}}$) can be distributed through the strut, in line with the nanoindentation results (Fig. 4); note that the post-deformation behaviors after nanoindentation (Fig. 4) exhibit a bending mode of deformation followed by buckling through the strut. As a result, the isotropic periodicity in the diamond-structured Au can distribute the applied stress through the neighboring struts equally and symmetrically; that might be one of the reasons for high mechanical properties with low density. Furthermore, the deformation mechanism was examined by investigating the plastic strain on the nanonetwork Au at different strains from 1%, 2%, 5%, and 10% as shown in Fig. 6d. As found, the deformation strain ($\varepsilon_{\text{plastic}}$) at 1% and 2% are within the elastic region; the computed strain clearly shows the strain maximization at the middle of the connective node; note that this might be attributed to the linear elasticity by bending of the strut. Furthermore, the nanonetwork Au exhibits plastic deformation at 5% and 10% of strain, the contours of equivalent plastic strain indicate the location of buckling and morphological rupture at plateau yield. As a result, the plastic deformation of well-ordered nanonetwork Au should occur through elastic bending of the strut followed by plastic buckling without any ligament slips; that is similar to the results reported by Biener et al. and also in line with the FESEM observations of post-indentation analysis. The mechanical enhancement from the deliberate structuring of nanonetwork textures for thermoset polymers fabricated by templated polymerization has been demonstrated by Ho et al. As reported in this article, the diamond-structured monolith is better than the one with gyroid, indicating that the higher number of struts in tetrahedral geometry is indeed superior in terms of mechanical performance than the trigonal planar geometry in gyroid. As a result, diamond-structured

nanonetwork Au was fabricated to scrutinize the mechanical properties of deliberate structuring of metals in the nanoscale.

In fact, the fabrication method can be extended into various nanonetwork materials with a high number of struts for the enhancement of the mechanical properties of network materials. Here, this study aims to enhance the mechanical properties of strut-based metallic materials even though it shows bending-dominated behavior; note that the bending-dominated structures can largely reduce the dependence of mechanical properties with density. As found in this study, the nanonetwork Au fabricated can show significant enhancement in reduced elastic modulus and yield strength above the upper limit of the Hashin-Shtrikman upper bound[14,54,55]. Accordingly, the nanonetwork Au fabricated can be used as a represented system of open-cell porous materials with high strength at low density for practical applications.

Conclusions

A well-ordered nanonetwork Au with precisely controlled nanoscale dimension can be fabricated by a bottom-up approach using a self-assembled block copolymer as a template for templated electrochemical deposition. The mechanical properties of the diamond-structured Au were examined by nanoindentation and micro-compression tests, showing superior reduced elastic modulus and yield strength based on material property-density plots using the scaling law proposed by Gibson and Ashby even though the fabricated networks are bending-dominated cellular material. The deformation mechanism of the nanonetwork Au was bending-dominated as evidenced by FESEM imaging experimentally and by numerical simulation using FEA at which the applied stress can be distributed equally through the struts. The enhanced mechanical performances are attributed to the combined effects of deliberate structuring with diamond network texture and nanosized ligaments in the well-ordered Au fabricated in this study.

Acknowledgements
We thank the Ministry of Science and Technology of the Republic of China, Taiwan, for financially supporting this research under MOST 110-2124-M-007-001, MOST 107-2923-M-007-003-MY3, MOST 108-2221-E-007-054 -MY3, MOST 108-2221-E-007-081-MY3, and MOST 109-2124-M-006 -003. We also thank The National Synchrotron Radiation Research Center (NSRRC, Taiwan) for its assistance in the Synchrotron SAXS experiments.

Author details
[1]Department of Chemical Engineering, National Tsing Hua University, Hsinchu 30013, Taiwan. [2]Department of Power Mechanical Engineering, National Tsing Hua University, Hsinchu 30013, Taiwan. [3]Department of Material Science and Engineering, National Tsing Hua University, Hsinchu 30013, Taiwan. [4]Department of Material Science and Engineering, National Taiwan University, Taipei 10617, Taiwan

Author contributions
S.K.S. conceived and designed the experiments. S.K.S., H.S., C.-W.W., C.-Y.T., and C.-L.L. obtained experimental data. C.-W.W. performed theoretical calculations. S.K.S., and H.S. analyzed the experimental and theoretical results. C.-C.L., S.-Y.C., C.-H.H. and R.-M.H. supervised the entire project.

Conflict of interest
The authors declare no competing interests.

Publisher's note
Springer Nature remains neutral with regard to jurisdictional claims in published maps and institutional affiliations.

Supplementary information The online version contains supplementary material available at https://doi.org/10.1038/s41427-023-00483-y.

Received: 21 February 2023 Revised: 4 May 2023 Accepted: 15 May 2023
Published online: 23 June 2023

References

1. Gibson, L. J., Ashby, M. F. & Harley, B. A. *Cellular Materials in Nature and Medicine* (Cambridge University Press, 2010).
2. Yang, T. et al. High strength and damage-tolerance in echinoderm stereom as a natural bicontinuous ceramic cellular solid. *Nat. Commun.* **13**, 1–12 (2022).
3. Yang, T. et al. A damage-tolerant, dual-scale, single-crystalline microlattice in the knobby starfish, Protoreaster nodosus. *Science* **375**, 647–652 (2022).
4. Zhao, H., Yang, Z. & Guo, L. Nacre-inspired composites with different macroscopic dimensions: strategies for improved mechanical performance and applications. *NPG Asia Mater.* **10**, 1–22 (2018).
5. Yu, X., Zhou, J., Liang, H., Jiang, Z. & Wu, L. Mechanical metamaterials associated with stiffness, rigidity and compressibility: a brief review. *Prog. Mater. Sci.* **94**, 114–173 (2018).
6. Deshpande, V. S., Ashby, M. F. & Fleck, N. A. Foam topology: Bending versus stretching dominated architectures. *Acta Mater.* **49**, 1035–1040 (2001).
7. Nicolaou, Z. G. & Motter, A. E. Mechanical metamaterials with negative compressibility transitions. *Nat. Mater.* **11**, 608–613 (2012).
8. Kadic, M., Milton, G. W., van Hecke, M. & Wegener, M. 3D metamaterials. *Nat. Rev. Phys.* **1**, 198–210 (2019).
9. Pendry, J. B., Schurig, D. & Smith, D. R. Controlling electromagnetic fields. *Science* **312**, 1780–1782 (2006).
10. Pendry, J. B., Holden, A. J., Stewart, W. J. & Youngs, I. Extremely low frequency plasmons in metallic mesostructures. *Phys. Rev. Lett.* **76**, 4773–4776 (1996).
11. Lee, J. H., Wang, L., Kooi, S., Boyce, M. C. & Thomas, E. L. Enhanced energy dissipation in periodic epoxy nanoframes. *Nano Lett.* **10**, 2592–2597 (2010).
12. Frenzel, T., Kadic, M. & Wegener, M. Three-dimensional mechanical metamaterials with a twist. *Science* **358**, 1072–1074 (2017).
13. Kagias, M. et al. Metasurface-Enabled Holographic Lithography for Impact-Absorbing Nanoarchitected Sheets. *Adv. Mater.* **35**, 2209153 (2023).
14. Bauer, J., Hengsbach, S., Tesari, I., Schwaiger, R. & Kraft, O. High-strength cellular ceramic composites with 3D microarchitecture. *Proc. Natl Acad. Sci.* **111**, 2453–2458 (2014).
15. Hakamada, M. & Mabuchi, M. Mechanical strength of nanoporous gold fabricated by dealloying. *Scr. Mater.* **56**, 1003–1006 (2007).
16. Li, X. & Gao, H. Mechanical metamaterials: smaller and stronger. *Nat. Mater.* **15**, 373–374 (2016).
17. Biener, J. et al. Size effects on the mechanical behavior of nanoporous Au. *Nano Lett.* **6**, 2379–2382 (2006).
18. Biener, J. et al. Nanoporous plasmonic metamaterials. *Adv. Mater.* **20**, 1211–1217 (2008).
19. Chiu, P. T. et al. Gold nanohelices for chiral plasmonic films by templated electroless plating. *Adv. Opt. Mater.* **9**, 2002133 (2021).
20. Surjadi, J. U. et al. Mechanical metamaterials and their engineering applications. *Adv. Eng. Mater.* **21**, 1800864 (2019).
21. Jo, S. et al. Symmetry-breaking in double gyroid block copolymer films by non-affine distortion. *Appl. Mater. Today* **23**, 101006 (2021).
22. Zheng, X. et al. Ultralight, ultrastiff mechanical metamaterials. *Science* **344**, 1373–1377 (2014).

23. Schaedler, T. A. et al. Ultralight metallic microlattices. *Science* **334**, 962–965 (2011).
24. Hsueh, H. Y. et al. Well-defined multibranched gold with surface plasmon resonance in near-infrared region from seeding growth approach using gyroid block copolymer template. *Adv. Mater.* **25**, 1780–1786 (2013).
25. Bates, F. S. & Fredrickson, G. H. Block copolymer thermodynamics: theory and experiment. *Annu. Rev. Phys. Chem.* **41**, 525–557 (1990).
26. Bates, F. S. et al. Fluctuations, conformational asymmetry and block copolymer phase behaviour. *Faraday Discuss* **98**, 7–18 (1994).
27. Al-Ketan, O. et al. Microarchitected stretching-dominated mechanical metamaterials with minimal surface topologies. *Adv. Eng. Mater.* **20**, 1800029 (2018).
28. Siddique, S. K. et al. Nanonetwork thermosets from templated polymerization for enhanced energy dissipation. *Nano Lett.* **21**, 3355–3363 (2021).
29. Sadek, H. et al. Bioinspired nanonetwork hydroxyapatite from block copolymer templated synthesis for mechanical metamaterials. *ACS Nano* **16**, 18298–18306 (2022).
30. Cheng, C. F. et al. Nanoporous gyroid platinum with high catalytic activity from block copolymer templates via electroless plating. *NPG Asia Mater.* **7**, e170–e170 (2015).
31. Yang, K. C. et al. Single gyroid-structured metallic nanoporous spheres fabricated from double gyroid-forming block copolymers via templated electroless plating. *NPG Asia Mater.* **11**, 1–11 (2019).
32. Hsueh, H. Y., Yao, C. T. & Ho, R. M. Well-ordered nanohybrids and nanoporous materials from gyroid block copolymer templates. *Chem. Soc. Rev.* **44**, 1974–2018 (2015).
33. Li, F. et al. Highly porous metal oxide networks of interconnected nanotubes by atomic layer deposition. *Nano Lett.* **12**, 5033–5038 (2012).
34. Yang, K. C., Puneet, P., Chiu, P. T. & Ho, R. M. Well-ordered nanonetwork metamaterials from block copolymer templated syntheses. *Acc. Chem. Res.* **55**, 2033–2042 (2022).
35. Lee, T. L., Lin, J. W. & Ho, R. M. Controlled self-assembly of polystyrene- block-polydimethylsiloxane for fabrication of nanonetwork silica monoliths. *ACS Appl. Mater. Interfaces* **14**, 54194–54202 (2022).
36. Georgopanos, P., Lo, T. Y., Ho, R. M. & Avgeropoulos, A. Synthesis, molecular characterization and self-assembly of (PS-: B -PDMS)n type linear (n = 1, 2) and star (n = 3, 4) block copolymers. *Polym. Chem.* **8**, 843–850 (2017).
37. Gibson, L. J. Cellular solids. *MRS Bull.* **28**, 270–274 (2003).
38. Dong, L., Deshpande, V. & Wadley, H. Mechanical response of Ti-6Al-4V octet-truss lattice structures. *Int. J. Solids Struct.* **60**, 107–124 (2015).
39. Jacobsen, A. J., Barvosa-Carter, W. & Nutt, S. Micro-scale truss structures formed from self-propagating photopolymer waveguides. *Adv. Mater.* **19**, 3892–3896 (2007).
40. Meza, L. R., Das, S. & Greer, J. R. Strong, lightweight, and recoverable three-dimensional ceramic nanolattices. *Science* **345**, 1322–1326 (2014).
41. Greer, J. R. & De Hosson, J. T. M. Plasticity in small-sized metallic systems: Intrinsic versus extrinsic size effect. In *Prog. Mater. Sci.* **56**, 654–724 (2011).
42. Mieszala, M. et al. Micromechanics of amorphous metal/polymer hybrid structures with 3D cellular architectures: size effects, buckling behavior, and energy absorption capability. *Small* **13**, 1602514 (2017).
43. Biener, J., Hodge, A. M., Hamza, A. V., Hsiung, L. M. & Satcher, J. H. Nanoporous Au: a high yield strength material. *J. Appl. Phys.* **97**, 24301 (2005).
44. Hodge, A. M., Hayes, J. R., Caro, J. A., Biener, J. & Hamza, A. V. Characterization and mechanical behavior of nanoporous gold. *Adv. Eng. Mater.* **8**, 853–857 (2006).
45. Hodge, A. M. et al. Scaling equation for yield strength of nanoporous open-cell foams. *Acta Mater.* **55**, 1343–1349 (2007).
46. Khaderi, S. N. et al. The indentation response of Nickel nano double gyroid lattices. *Extrem. Mech. Lett.* **10**, 15–23 (2017).
47. Yang, L. et al. Insights into unit cell size effect on mechanical responses and energy absorption capability of titanium graded porous structures manufactured by laser powder bed fusion. *J. Mech. Behav. Biomed. Mater.* **109**, 103843 (2020).
48. Cheng, I. C. & Hodge, A. M. Strength scale behavior of nanoporous Ag, Pd and Cu foams. *Scr. Mater.* **69**, 295–298 (2013).
49. Wendy, G. X. & Greer, J. R. Ultra-strong architected Cu meso-lattices. *Extrem. Mech. Lett.* **2**, 7–14 (2015).
50. Biener, M. M. et al. ALD functionalized nanoporous gold: thermal stability, mechanical properties, and catalytic activity. *Nano Lett.* **11**, 3085–3090 (2011).
51. Volkert, C. A., Lilleodden, E. T., Kramer, D. & Weissmüller, J. Approaching the theoretical strength in nanoporous Au. *Appl. Phys. Lett.* **89**, 61920 (2006).
52. Ye, X. L. & Jin, H. J. Corrosion-induced strengthening: development of high-strength nanoporous metals. *Adv. Eng. Mater.* **18**, 1050–1058 (2016).
53. Biener, J., Hodge, A. M. & Hamza, A. V. Microscopic failure behavior of nanoporous gold. *Appl. Phys. Lett.* **87**, 1–3 (2005).
54. Jang, D., Meza, L. R., Greer, F. & Greer, J. R. Fabrication and deformation of three-dimensional hollow ceramic nanostructures. *Nat. Mater.* **12**, 893–898 (2013).
55. Montemayor, L. C., Meza, L. R. & Greer, J. R. Design and fabrication of hollow rigid nanolattices via two-photon lithography. *Adv. Eng. Mater.* **16**, 184–189 (2014).